

pubs.acs.org/JACS Article

Synthetic Roadmap to a Large Library of Colloidal High-Entropy Rare Earth Oxyhalide Nanoparticles Containing up to Thirteen Metals

Charles H. Wood and Raymond E. Schaak*



Cite This: J. Am. Chem. Soc. 2024, 146, 18730–18742



ACCESS I

III Metrics & More

Article Recommendations

Supporting Information

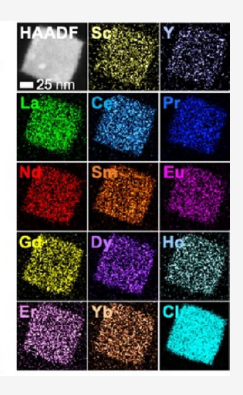
ABSTRACT: Nanoparticles of high-entropy materials that incorporate five or more elements randomized on a crystalline lattice often exhibit synergistic properties that can be influenced by both the identity and number of elements combined. These considerations are especially important for structurally and compositionally complex materials such as multimetal multianion compounds, where cation and anion mixing can influence properties in competitive and contradictory ways. Here, we demonstrate the synthesis of a large library of colloidal highentropy rare earth oxyhalide (REOX) nanoparticles. We begin with the synthesis of (LaCePrNdSmEuGdDyHoErYbScY)OCl, which homogeneously incorporates 13 distinct rare earth elements. Through time point studies, we find that (LaNdSmGdDy)OCl, a

high-entropy REOCI nanoparticles

13 of 1,287 5-metal options

(LaCePrNdSmEuGdDyHoErYbScY)OCI

7,099-member library of



5-metal analogue, forms through *in situ* generation of compositionally segregated core@shell@shell intermediates that convert to homogeneously mixed products through apparent core—shell interdiffusion. Assuming that all possible combinations of 5 through 13 rare earth metals are synthetically accessible, we propose the existence of a 7099-member *REOCl* nanoparticle library, of which we synthesize and characterize 40 distinct members. We experimentally validate the incorporation of a large number of rare earth elements using energy dispersive X-ray spectra, despite closely spaced and overlapping X-ray energy lines, using several fingerprint matching strategies to uniquely correlate experimental and simulated spectra. We confirm homogeneous mixing by analyzing elemental distributions in high-entropy nanoparticles versus physical mixtures of their constituent compounds. Finally, we characterize the band gaps of the 5- and 13-metal *REOCl* nanoparticles and find a significantly narrowed band gap, relative to the constituent *REOCl* phases, in (LaCePrNdSmEuGdDyHoErYbScY)OCl but not in (LaNdSmGdDy)OCl.

■ INTRODUCTION

High-entropy materials have complex compositions that lead to unique properties in many application areas that include catalysis, batteries, proton and ionic conductors, magnetism, and thermoelectrics. A high-entropy material is typically defined as a solid solution having five or more elements that are randomly mixed, in near-equimolar ratios, throughout a crystal structure. This large number of randomly mixed elements leads to synergistic interactions through the so-called "cocktail effect" that modifies fundamental material properties, including electronic structure, band gap, chemical reactivity, and catalytic activity and selectivity. Colloidal nanoparticles of high-entropy materials are especially useful for systems that could exhibit size- or shape-dependent properties and for applications that could benefit from high surface areas and/or solution processability. 13–15

Generally, high-entropy materials are synthesized at high temperatures, which maximizes the magnitude of the entropy term in the Gibbs free energy equation, and then quenched to trap the uniformly mixed phase that is stable at high temperatures. 16-18 Such high-temperature approaches are generally incompatible with colloidal nanocrystal synthesis, which is limited to solvent-accessible temperatures. 13 Colloidal methods for the synthesis of high-entropy nanoparticles are emerging and have produced alloys, intermetallic compounds, chalcogenides, oxides, and oxychalcogenides. 14,19-27 However, the chemical pathways that lead to their formation are often complex. 13,14 While traditionally assumed to be one-step reactions that conucleate and grow nanoparticles of the high-entropy material directly, it is becoming clear that multistep pathways are often involved. 13,14,27,28 These pathways often integrate different types of reactions, simultaneously and/or in

Received: May 13, 2024 Revised: June 14, 2024 Accepted: June 17, 2024 Published: June 29, 2024





quick succession, to enable colocalization of the large number of elements within each nanoparticle.¹³

Nanoparticles of high-entropy mixed-anion compounds are particularly interesting synthetic targets, especially since anionsite mixing can modify properties in different ways than cationsite mixing. 23,29 As an example, a recent report on colloidal nanoparticles of the high-entropy lanthanide oxysulfide (Pr,Nd,Gd,Dy,Er)₂O₂S demonstrated quantum confinement effects that resulted in different optical properties than a bulk oxysulfide having the same composition. 23,29 The rare earth oxyhalides REOX, of which LaOCl is a prototypical member, are especially exciting high-entropy candidates. 30-35 The REOX compounds, which adopt the tetragonal matlockite PbFCl crystal structure, contain alternating bilayers of [REO]⁺ (RE = rare earth elements La-Lu, Sc, Y) and X^- (X = halides Cl, Br, and I). 36-38 LaOCl serves as a host for other rare earth cations, which impart luminescent and up-conversion properties that make them useful as phosphors. 32,36,39,40 LaOCl and related LaOX compounds have also been used as anion conductors, heterogeneous catalysts, and photoactive catalytic support materials. The band gap (E_g) of LaOCl has been reported to range from 5.53 to 5.83 eV, which classifies it as an ultrawide band gap material. 46,47 However, mixing of cations in high-entropy oxides is known to decrease band gaps relative to the parent compounds, as has been observed in spinel-type (FeCoNiCuZn)Al₂O₄ and in the rare earth oxide (CeGdLaNdPrSmY)O₂₋₀.48-50 High-entropy analogues of REOX therefore are fundamentally interesting targets, given the competition between the band structure features that lead to an ultrawide band gap in the oxyhalides versus potential band gap narrowing due to high-entropy cation mixing. 30-32

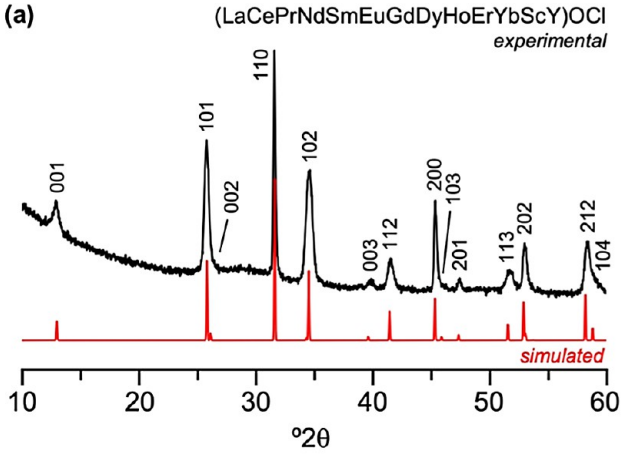
Here, we report the colloidal synthesis of a library of highentropy REOX nanoparticles. We begin with (LaCePrNdSm-EuGdDyHoErYbScY)OCl, which contains 13 distinct rare earth elements colocalized within the nanoparticles. Given the successful synthesis of this 13-metal REOX compound, along with the assumption that all possible combinations of 5, 6, 7, 8, 9, 10, 11, 12, and 13 rare earth metals should also be synthetically accessible, we propose the existence of a colloidal high-entropy REOCl nanoparticle library containing up to 7099 distinct members; details are provided in the Supporting Information. We then synthesize and characterize 40 members of this REOCl nanoparticle library to validate the concept as well as an oxybromide analogue. Using (LaNdSmGdDy)OCl as a representative system, we probe the pathway by which the high-entropy REOX nanoparticles form and identify unexpected core@shell nanoparticle intermediates that progress, through apparent in situ core-shell interdiffusion, to the final high-entropy products. Finally, we characterize the band gaps of the representative 5- and 13-metal high-entropy REOCl samples. We find that the band gap of (LaNdSmGdDy)OCl is a weighted average of its constituent single-metal compounds, while that of (LaCePrNdSmEuGdDyHoErYbScY)OCl is much narrower than previously reported REOCl compounds.

It is important to acknowledge that for compositionally complex nanoparticles containing such a large number of rare earth elements, characterization is challenging, particularly from the perspective of validating colocalization and alloying. 13,51-53 Given this challenge, we pay close attention to the deconvolution of closely spaced and overlapping X-ray energy lines in energy dispersive X-ray spectroscopy (EDS) data, which is the primary way by which element colocalization in high-entropy nanoparticles is validated in the literature. 3,13,19-21,53 We construct a series of control samples as well as fingerprint matching of complex EDS spectra to validate the reliability of the analysis. This approach helps to establish a roadmap for the routine microscopic characterization of compositionally complex nanoparticles that incorporate large numbers of elements having similar X-ray energies, which otherwise complicate reliable analysis.

RESULTS AND DISCUSSION

Synthesis and Characterization of (LaCePrNd-SmEuGdDyHoErYbScY)OCI. We began by synthesizing (LaCePrNdSmEuGdDyHoErYbScY)OCl, a high-entropy REOCl compound with 13 rare earth elements. To make this high-entropy compound, a heated mixture of each of the 13 constituent RECl₃ salts in oleylamine was rapidly injected into oleylamine at 330 °C to ensure simultaneous mixing of all rare earth metal cations. After 1 h of heating at 330 °C, the reaction was quenched, and the product was isolated. Complete details, which represent modifications of literature procedures for LaOCl, 39,54 are provided in the Experimental

Figure 1a shows experimental powder X-ray diffraction (XRD) data for the (LaCePrNdSmEuGdDyHoErYbScY)OCl nanoparticles, along with a simulated XRD pattern based on



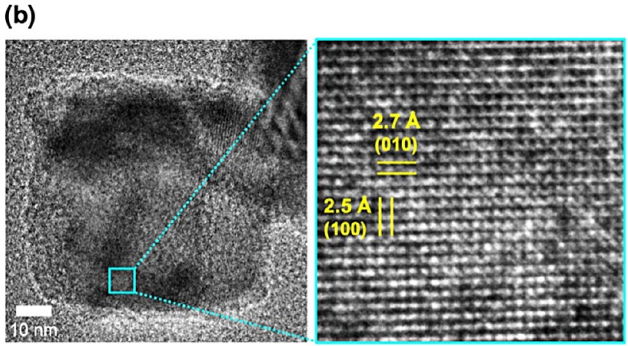


Figure 1. Characterization of REOCl nanoparticles containing 13 rare earth metals. (a) Experimental and simulated powder XRD patterns for high-entropy REOCl nanoparticles that contain 13 rare earth elements, (LaCePrNdSmEuGdDyHoErYbScY)OCl. The simulated reference pattern was generated using lattice constants that were determined empirically from the analysis of the XRD pattern. (b) HRTEM image of a single (LaCePrNdSmEuGdDyHoErYbScY)OCl particle along with an enlarged region that shows the lattice spacings and planes.

the structure of LaOCl. 55 The experimental pattern matches well with a single-phase pattern that was generated based on the tetragonal matlockite structure of LaOCl with empirically determined lattice constants of a = 4.00 Å and c = 6.77 Å. These lattice constants are intermediate between those of the largest end member (LaOCl, a = 4.11 Å and c = 6.87 Å) and the smallest end member (ScOCl, a = 4.32 Å and c = 5.64Å).^{37,55} No crystalline impurities are evident. Scherrer analysis of the (001) peak in the XRD pattern in Figure 1 indicates a grain size of around 13 nm. However, peak widths vary and many of the peaks are much sharper, corresponding to larger grain sizes. Such behavior is characteristic of anisotropic grains, such as plates, which are thinner in one direction and thicker in others.⁵⁶ Consistent with the XRD data, Figure 1b shows a high-resolution transmission electron microscopy (HRTEM) image of the nanoparticles that were isolated from the reaction, which form as polydisperse plates that range in diameter from approximately 50 to 200 nm. Analysis of the accompanying lattice-resolved image in Figure 1b reveals perpendicular spacings of 2.5 and 2.7 Å, which correspond to the (100) and (010) planes, respectively. These lattice spacings indicate that the particle is oriented in the [001] direction, which is consistent with the XRD data in Figure 1a. In particular, the particle morphology and orientation are consistent with broader peaks for all (hkl) reflections containing a nonzero l value and sharper peaks for all (h00), (0k0), and (hk0) reflections.

Figure 2a shows a high angle annular dark field (HAADF) STEM image, along with the corresponding STEM-EDS element maps, for a single REOCl particle. Visually, the STEM-EDS element maps suggest that all 13 rare earth elements are present and colocalized within the REOCl particle. A line scan shown in Figure 2b, acquired from the region of the HAADF-STEM image indicated by the arrow, confirms that all 13 rare earth elements have an above-baseline signal and uniform distribution across the particle. Figure 2c shows a bar chart, with error bars generated from three data sets, corresponding to the average composition of all elements (except oxygen) based on analysis of the single-particle STEM-EDS maps as well as an enlarged region showing only the rare earth elements. Analysis of the data in Figure 2c leads to a composition of $La_{0.09}Ce_{0.12}Pr_{0.09}Nd_{0.08}Sm_{0.11}Eu_{0.06}Gd_{0.08}Dy_{0.09}$ $Ho_{0.03}Er_{0.05}Yb_{0.10}Sc_{0.03}Y_{0.05}OCl$ based on the average of the single-particle analyses and fixing the overall stoichiometry to REOCl. This analysis also confirms that all 13 rare earth elements are present and colocalized.

An ensemble EDS spectrum, corresponding to a collection of REOCl particles, is shown in Figure 3a, along with an enlarged region that emphasizes the rare earth elements in Figure 3b. The experimental EDS spectrum is shown, along with a simulated EDS spectrum generated based on the EDSdetermined composition of the REOCl sample. Color-coded lines corresponding to the energies and intensities of each Xray line that comprise the simulated spectrum are also shown. The composition determined from this larger-area EDS analysis is $La_{0.08}Ce_{0.09}Pr_{0.07}Nd_{0.07}Sm_{0.10}Eu_{0.07}Gd_{0.08}$ $Dy_{0.09}Ho_{0.06}Er_{0.07}Yb_{0.09}Sc_{0.05}Y_{0.08}OCl$, which matches well with that determined from the average of several individual particles presented in Figure 2. Given this consistent composition, we can consider how the composition determined from TEM matches the composition from XRD based on Vegard's law. Using Vegard's law, the weighted average of lattice constants based on the average composition

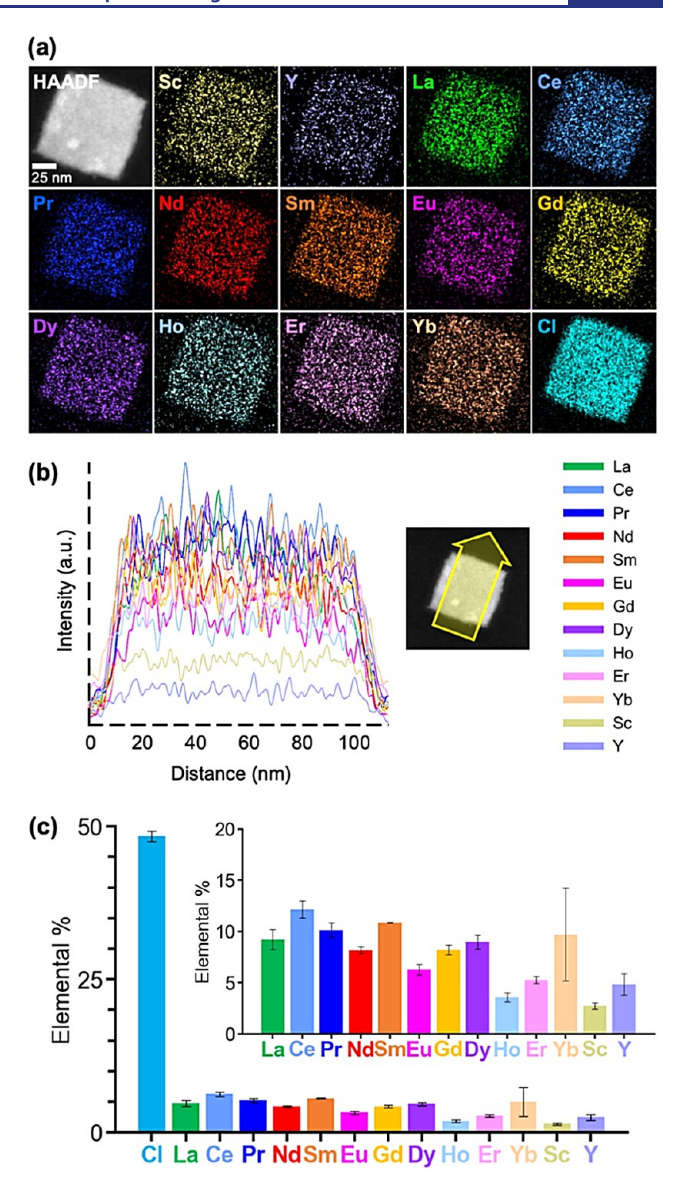
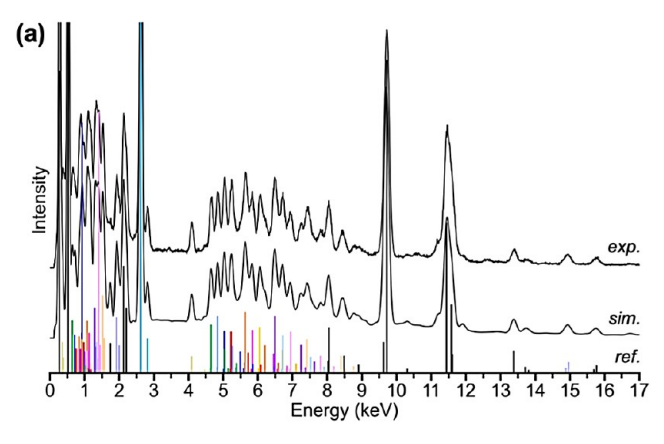


Figure 2. Composition analysis of REOCl nanoparticles containing 13 rare earth elements. (a) HAADF-STEM image of a single (LaCe-PrNdSmEuGdDyHoErYbScY)OCl nanoparticle, along with the corresponding overlaid STEM-EDS element maps for La, Ce, Pr, Nd, Sm, Eu, Gd, Dy, Ho, Er, Yb, Sc, Y, and Cl. (b) STEM-EDS line scan across the particle in panel (a). The yellow arrow indicates the region included in the line scan. The corresponding intensity profile for each element is plotted according to the color key. (c) Histogram (based on analysis of ensemble EDS data) showing the percentages of each element; average values and error bars are based on the analysis of three images. Chlorine is included in the main plot, while the inset shows only the rare earth elements.

given by quantitative analysis predicts lattice parameters of a =3.99 Å and c = 6.66 Å. These lattice parameters compare favorably to the empirically determined lattice parameters a =4.00 Å and c = 6.77 Å, which were used to generate the reference pattern in Figure 1.

Control Experiments and Analyses for Validating Composition and Element Colocalization. When analyzing the composition and elemental colocalization of compositionally complex nanoparticles using EDS and STEM-EDS, as we have done above and as is common in the literature, 2,13,14,51-53,57 it is imperative to ensure the validity



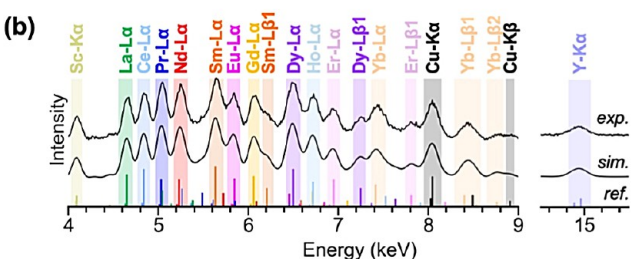


Figure 3. EDS composition analysis of the 13-element REOCl nanoparticle. (a) Ensemble EDS spectra (experimental, simulated, and reference) corresponding to a collection of (LaCePrNdSm-EuGdDyHoErYbScY)OCl nanoparticles. Simulated and reference spectra are generated using a composition-weighted model that contains La, Ce, Pr, Nd, Sm, Eu, Gd, Dy, Ho, Er, Yb, Sc, Y, and Cl, along with Au, C, O, Zr, Cu, and Ni (from the TEM grid plus adventitious signals from TEM). The colors for the elements in the REOCl nanoparticles correspond to the colors used in the line scan and histogram in Figure 2. (b) Enlarged region of the EDS spectra in panel (a), highlighting the energy ranges where the rare earth element lines are located. Highlighted regions correspond to the diagnostic peak(s) of each rare earth element.

of the data and the reliability of the analysis. For the REOCl particles that contain 13 rare earth elements, this requirement is especially important to consider. 13 The large number of EDS lines and their energies complicates this process, since they are sufficiently close to one another that they overlap. 13 Peak deconvolution is therefore necessary. Implemented incorrectly, peak deconvolution can lead to elemental compositions and spatial distributions that are inaccurate and even erroneous, including the observation of signals that are not real and maps that show the presence of elements in regions where they are not.13

Overlap of the key peaks in the EDS spectrum for the REOCl particles is evident in the color-coded line spectra that comprise the simulated EDS spectrum in Figure 3. We address this challenge for 13-element REOCl nanoparticles in three ways. First, we validate that the simulated EDS spectrum, which combines the multipeak profiles from all 13 rare earth elements, represents a unique fingerprint that matches the experimental spectrum with sufficient accuracy that even 12element combinations cannot achieve. Second, we confirm accurate spatial distributions during elemental mapping by generating control samples containing physical mixtures of the constituent single-metal REOCl nanoparticles, demonstrating the ability to accurately discern between colocalization and segregation. Third, we systematically remove one rare earth element at a time to form samples of REOCl nanoparticles that each have 12, 11, 10, 9, 8, 7, 6, 5, 4, 3, 2, or 1 rare earth element and then confirm that each of these has a unique EDS spectrum (and corresponding STEM-EDS element map) that matches the compositions and colocalization expected based on the synthesis. These three sets of controls provide confidence in the EDS analysis given the compositional complexity of these nanoparticles.

We began by evaluating the validity of the simulated EDS spectrum, as shown in Figure 3. One approach is to assume that the simulated EDS spectrum, which incorporates multiple closely spaced EDS lines for each of the 13 constituent elements of the high-entropy REOCl nanoparticles, represents a unique fingerprint. If this is a valid assumption, then alternative simulated EDS spectra containing any combination of 12 of the 13 constituent elements should not match the experimental data. Put another way, by removing any one of the constituent rare earth elements, the simulated EDS spectrum should change enough to be visibly different than the experimental spectrum. Figure 4 shows 14 individual panels that all contain the same experimental EDS spectrum for the REOCl sample having 13 rare earth elements, along with different simulated EDS spectra; only the regions from 4 to 9 and 14.5-15.5 keV are shown, as these contain the most characteristic peaks for the collection of rare earth elements. As shown in Figure 3b and again in the first panel of Figure 4 for comparison, the simulated spectrum containing all 13 elements matches well with the experimental spectrum. The other panels in Figure 4 each exclude one of the 13 elements from the model used to generate the simulated spectrum. The vertical color-coded lines in each panel indicate where the primary peak(s) for each missing element should appear. Inspection of all simulated spectra confirms that the only model that uniquely matches the experimental data is the one containing all 13 rare earth elements; it is indeed a unique fingerprint that cannot be matched by any of the 12-element combinations.

Given our confidence in the composition based on our analysis of the ensemble EDS spectrum, we turn to the challenge of validating accurate spatial distributions of the elements in the STEM-EDS maps. To address this issue, we prepared two distinct samples for identical analysis by STEM-EDS element mapping. First, we synthesized six REOCl nanoparticle samples that each contained only a single rare earth element: LaOCl, PrOCl, NdOCl, SmOCl, GdOCl, and DyOCl. Characterization data for these samples are included in Figures S1 and S2 of the Supporting Information. We mixed these samples to create a combined sample that includes all six types of single-metal REOCl nanoparticles. We then used STEM-EDS to map and image this sample, focusing strategically on a region of LaOCl, PrOCl, NdOCl, SmOCl, and GdOCl nanoparticles; nanoparticles of DyOCl were purposely not present in this aggregate.

Figure 5a shows the HAADF-STEM image and the combined STEM-EDS element map that superimposes the signals corresponding to the La, Pr, Nd, Sm, Gd, and Dy L lines; the individual maps are also shown for comparison and to better visualize the spatial distributions of each element. Qualitatively, intense signals for the La, Pr, Nd, Sm, and Gd L lines segregate onto individual particles, while the weak signal from the Dy L lines overlaps with the signals from the Sm and Gd L lines. The weak signal from the Pr L lines also overlaps with the signal from the La L lines. These overlapping signals are expected, since their EDS lines partially overlap, but here, it is important to look at the intensities of the signals and not just

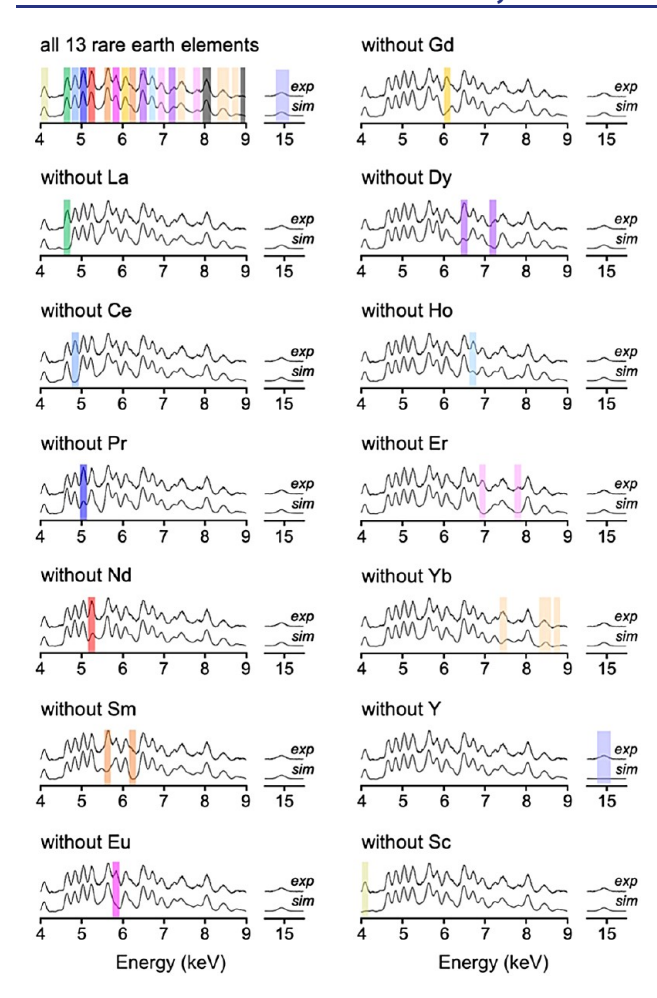


Figure 4. Comparative EDS composition analysis of 13-element REOCl nanoparticles. Each panel shows the same experimental EDS spectrum for the (LaCePrNdSmEuGdDyHoErYbScY)OCl nanoparticles that is shown in Figure 3b, along with different simulated spectra for comparison. The first panel, which contains a simulated spectrum that includes all 13 rare earth elements, is identical with that shown in Figure 3b. The subsequent panels each exclude one of the 13 elements from the model used to generate the simulated spectrum and highlight the diagnostic peak(s) that are modified due to each excluded element in the simulated spectrum. Each excluded element modifies the simulated EDS spectrum enough to make it detectably different from the experimental spectrum, resulting in an adequate match between simulated and experimental spectra only for the model that incorporates all 13 rare earth elements.

where they appear on the maps. Closer inspection of all individual STEM-EDS maps reveals similar weak background signals for most of the elements across all particles, although it is clear that the most intense signals are localized to distinct particles. Weak background signals for all elements are again expected because of how closely spaced the EDS lines are. That said, Figure 5b shows the EDS spectra acquired from each individual particle, as indicated by the colored boxes in Figure 5a. These spectra do not reveal above-background levels of other elements in each region beyond those that are expected to be present. The ensemble EDS spectrum, which corresponds to the entire field of view that contains all particles, includes contributions from La, Pr, Nd, Sm, and Gd, while the individual point spectra for the indicated regions show contributions from only one rare earth element on each particle. Dy is missing, which is consistent with our purposeful

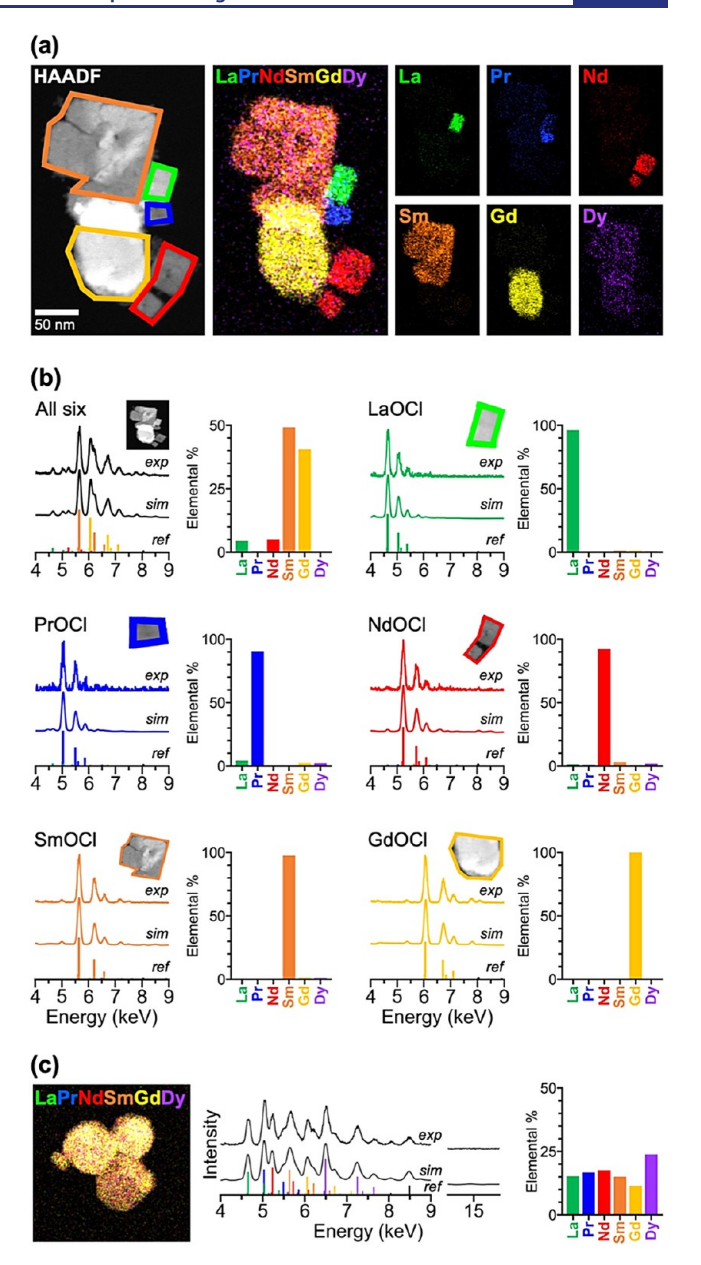


Figure 5. Analysis of compositionally analogous high-entropy and phase-segregated REOCl nanoparticles. (a) HAADF-STEM image of a sample generated from a physical mixture of LaOCl, PrOCl, NdOCl, SmOCl, GdOCl, and DyOCl nanoparticles, along with a corresponding STEM-EDS element map that superimposes the signals for the La, Pr, Nd, Sm, Gd, and Dy L lines. The individual STEM-EDS elemental maps are also shown. (b) Experimental, simulated, and reference EDS spectra, along with corresponding elemental percentage histograms acquired from analysis of the regions of the STEM-EDS maps shown in the insets, for the physical mixture as well as each individual particle, as indicated by the colored boxes and outlines. (c) STEM-EDS elemental map for high-entropy (LaPrNdSmGdDy)OCl nanoparticles, which contain the same rare earth metals as the physical mixture of REOCl nanoparticles in panel (a). Experimental, simulated, and reference EDS spectra are also shown for the ensemble of (LaPrNdSmGdDy)OCl nanoparticles as well as the corresponding elemental percentage histogram.

exclusion of DyOCl particles in the region that was imaged and analyzed.

The analysis described above indicates that "phantom" background signals in the STEM-EDS element maps are

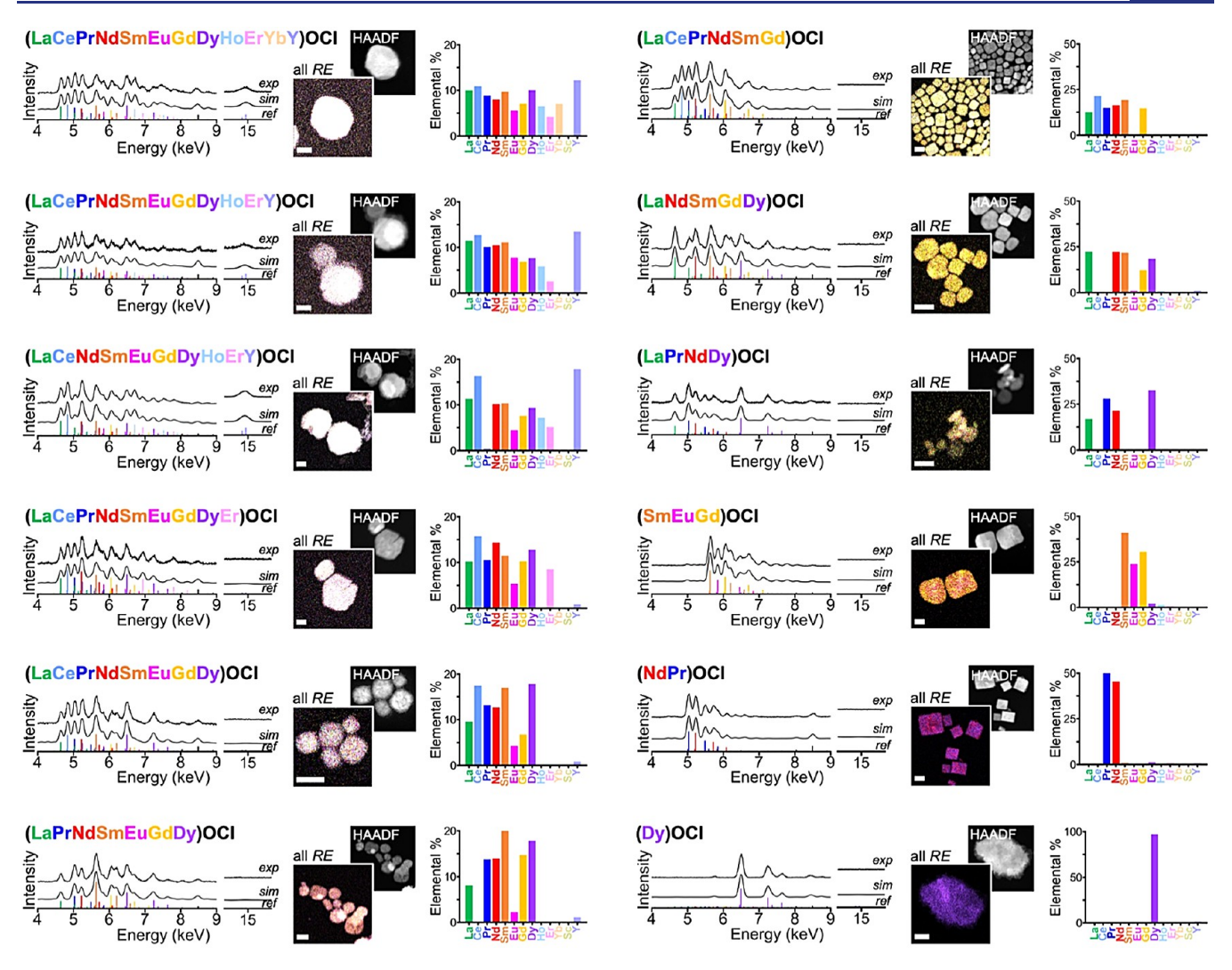


Figure 6. Characterization of *REOCI* nanoparticles that each include 12, 11, 10, 9, 8, 7, 6, 5, 4, 3, 2, or 1 rare earth element. Each panel contains experimental, simulated, and reference EDS spectra, a STEM-EDS element map showing all rare earth elements overlaid, a corresponding HAADF-STEM image, and an elemental percentage histogram confirming the presence of each targeted rare earth element. The simulated and reference spectra for each composition are generated by using a model that contains La, Ce, Pr, Nd, Sm, Eu, Gd, Dy, Ho, Er, Yb, Sc, Y, and Cl. All scale bars are 50 nm.

indeed present, as expected due to closely spaced EDS lines. However, they are present at background levels. These background-level signals do not contribute quantitatively to the relative ratios of the elements, and therefore, they are negligible when evaluating the composition. Furthermore, the corresponding bar charts in Figure 5b, which show the quantification of each individual EDS spectrum, indicate that the background levels of each potentially overlapping element all appear to be less than 5%, which validates the ability of our STEM-EDS analysis to accurately depict spatial distributions. As an additional comparison, Figure 5c shows a summary of analogous data for a sample of (LaPrNdSmGdDy)OCl, which is a high-entropy solid solution of all 6 rare earth elements. Here, all elements appear colocalized, as expected, confirming the ability to distinguish between phase-segregated and homogeneously mixed rare earth elements in this system. Individual STEM-EDS elemental maps are included in the Supporting Information (Figure S3).

Building on the control experiments and analyses described in Figures 3 and 4, we next synthesized a series of *REOCI* nanoparticles that systematically removed one rare earth element at a time from the starting 13-element (LaCePr-NdSmEuGdDyHoErYbScY)OCl system. Using this approach, we produced REOCl nanoparticle samples that each had 12, 11, 10, 9, 8, 7, 6, 5, 4, 3, 2, or 1 rare earth element and then confirmed that each of these had a unique EDS spectrum (and corresponding STEM-EDS element map) that matched the compositions and colocalization expected based on the synthesis. Figure 6 shows EDS data (both experimental and simulated), HAADF-STEM images, combined STEM-EDS element maps, and composition bar charts for (LaCePr-NdSmEuGdDyHoErYbY)OCl (12 RE), (LaCePrNdSmEuGd-DyHoErY)OCl (11 RE), (LaCeNdSmEuGdDyHoErY)OCl (10 RE), (LaCePrNdSmEuGdDyEr)OCl (9 RE), (LaCePr-NdSmEuGdDy)OCl (8 RE), (LaPrNdSmEuGdDy)OCl (7 RE), (LaCePrNdSmGd)OCl (6 RE), (LaNdSmGdDy)OCl (5 RE), (LaPrNdDy)OCl (4 RE), (SmEuGd)OCl (3 RE), (PrNd)OCl (2 RE), and (Dy)OCl (1 RE). Individual STEM-EDS elemental maps are included in the Supporting Information (Figure S4). The data in Figure 6 confirm that all REOCl samples have unique EDS spectra that match well with the simulated spectra based on their experimentally deter-

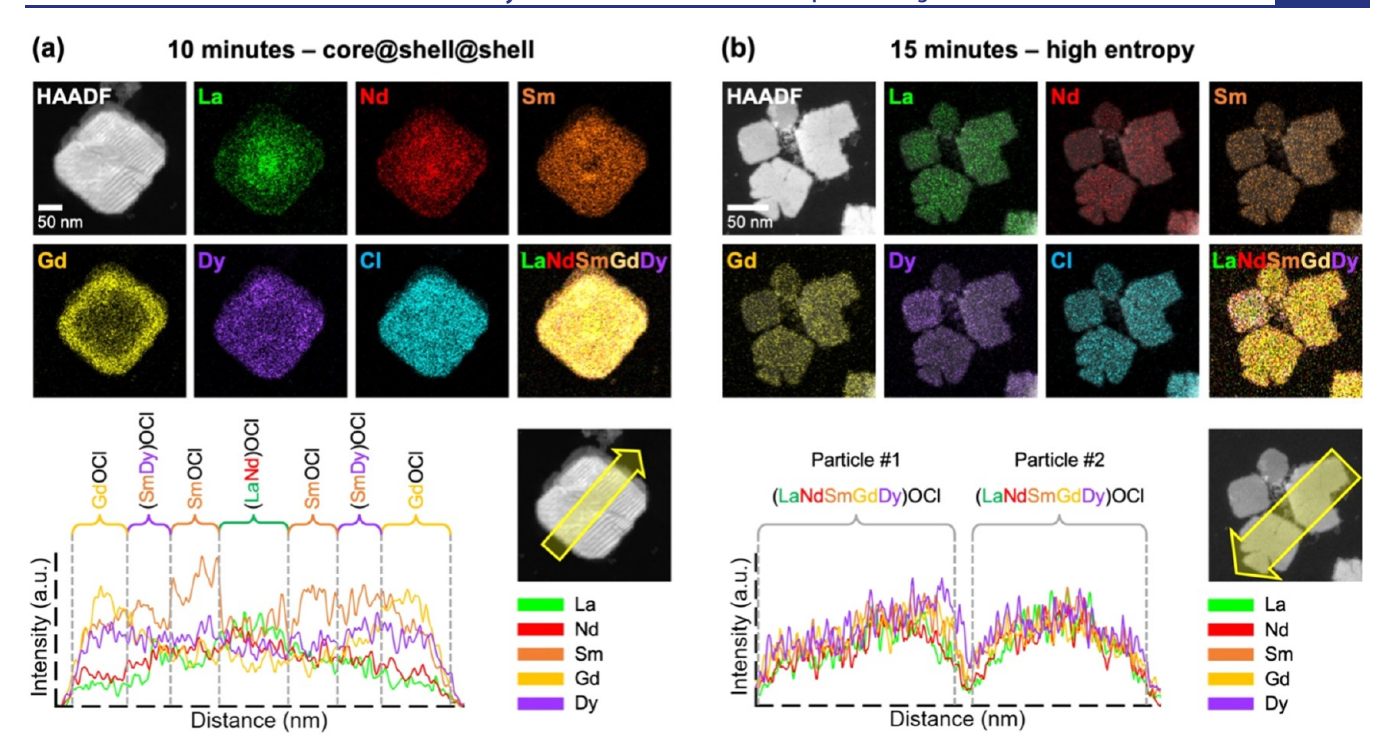


Figure 7. Temporal evolution of REOCl nanoparticle formation. Panels (a) and (b) correspond to (LaNdSmGdDy)OCl nanoparticle samples synthesized at 270 °C and isolated at 10 and 15 min, respectively. For both samples, HAADF-STEM images along with corresponding STEM-EDS element maps for La, Nd, Sm, Gd, Dy, Cl, and the combined rare earth elements are shown along with a line scan (corresponding to the yellow arrow) showing the spatial distribution of each rare earth element across the particles. The line scans are color-coded according to the key, and the distinct regions of the core@shell@shell intermediate (for the 10 min sample) or the distinct high-entropy particles (for the 15 min sample) are labeled.

mined composition, as well as the above-baseline presence of all expected elements and their colocalization within the particles.

Formation Pathway of High-Entropy REOCI Nanoparticles. Following the successful synthesis of REOCl nanoparticles that homogeneously incorporate up to 13 different rare earth metals, we wanted to understand how the high-entropy REOCl nanoparticles formed, given the apparent wide range of compositions that are potentially accessible.¹³ Accordingly, we probed the temporal evolution of composition during the synthesis of (LaNdSmGdDy)OCl, a high-entropy REOCl phase having five rare earth metals that was already shown in Figure 6 to form. (It is worth noting that the oxybromide analogue, (LaNdSmGdDy)OBr, can also be synthesized, as shown in Figure S5.) Our typical reaction temperature for the REOCl nanoparticles is 330 °C, but we confirmed that (LaNdSmGdDy)OCl can form as low as 270 °C (Figure S6). We therefore studied the temporal evolution of (LaNdSmGdDy)OCl at 270 °C so that the reaction would progress more slowly, allowing us to isolate any intermediate nanoparticles that formed in situ. Figure S7 shows powder XRD data for samples quenched at 5, 10, and 15 min after the rapid injection of the constituent RECl₃ reagent solution. At the earliest time point (5 min), XRD shows evidence for initial decomposition of the chloride salts, but the REOCl phases have not yet formed. By 10 min, and also at 15 min, the XRD pattern is consistent with a single REOCl phase that matches well with a simulated pattern having lattice constants calculated using Vegard's law for an equimolar solid solution containing all five rare earth metals (Figure S7). The XRD data therefore indicate that the reaction progresses quickly from

decomposition of the reagents to formation of the highentropy REOCl phase.

STEM-EDS analysis of the REOCl sample isolated at 10 min, shown in Figure 7a, reveals a surprising result. Despite the apparent single-phase XRD pattern in Figure S7, the STEM-EDS data indicate that some of the rare earth elements appear to be segregated. All five rare earth metals are present throughout the particle, as confirmed by the accompanying line scan. However, the center is rich in La and Nd, while Sm and Dy are enriched (relative to La and Nd) moving outward toward the edges of the particle. Most notably, Gd is richest around the perimeter of the particle. These three regions lead to an approximate core@shell@shell architecture that can be approximated as (La,Nd)OCl@(Sm,Dy)OCl@GdOCl. Even within this apparent core@shell@shell structure, there are gradients and mixing among the regions, which along with the broadened peaks, results in an apparent single-phase XRD pattern (based on lattice parameters), while STEM-EDS analysis indicates some segregation. By 15 min (Figure 7b), all five rare earth elements are colocalized and we see no evidence for the type of segregation that was observed in the 10 min sample. This suggests that as the reaction progresses, the rare earth elements interdiffuse, transforming from the core@shell@shell architecture to a homogeneous solid solution. This rapid interdiffusion process at 270 °C is unexpected, given the 3+ charge of the rare earth cations and the strong nature of the bonding in the RE-O layers.

We rationalize this pathway by considering the formation enthalpies ($\Delta H_{\rm f}^{\circ}$) of the constituent *REOCl* compounds. LaOCl, which has been reported to have the most negative $\Delta H_{\rm f}^{\circ}$ of -241.6 kcal/mol, is enriched in the center, along with NdOCl, which has a similar $\Delta H_{\rm f}^{\circ}$ of -239.0 kcal/mol. The

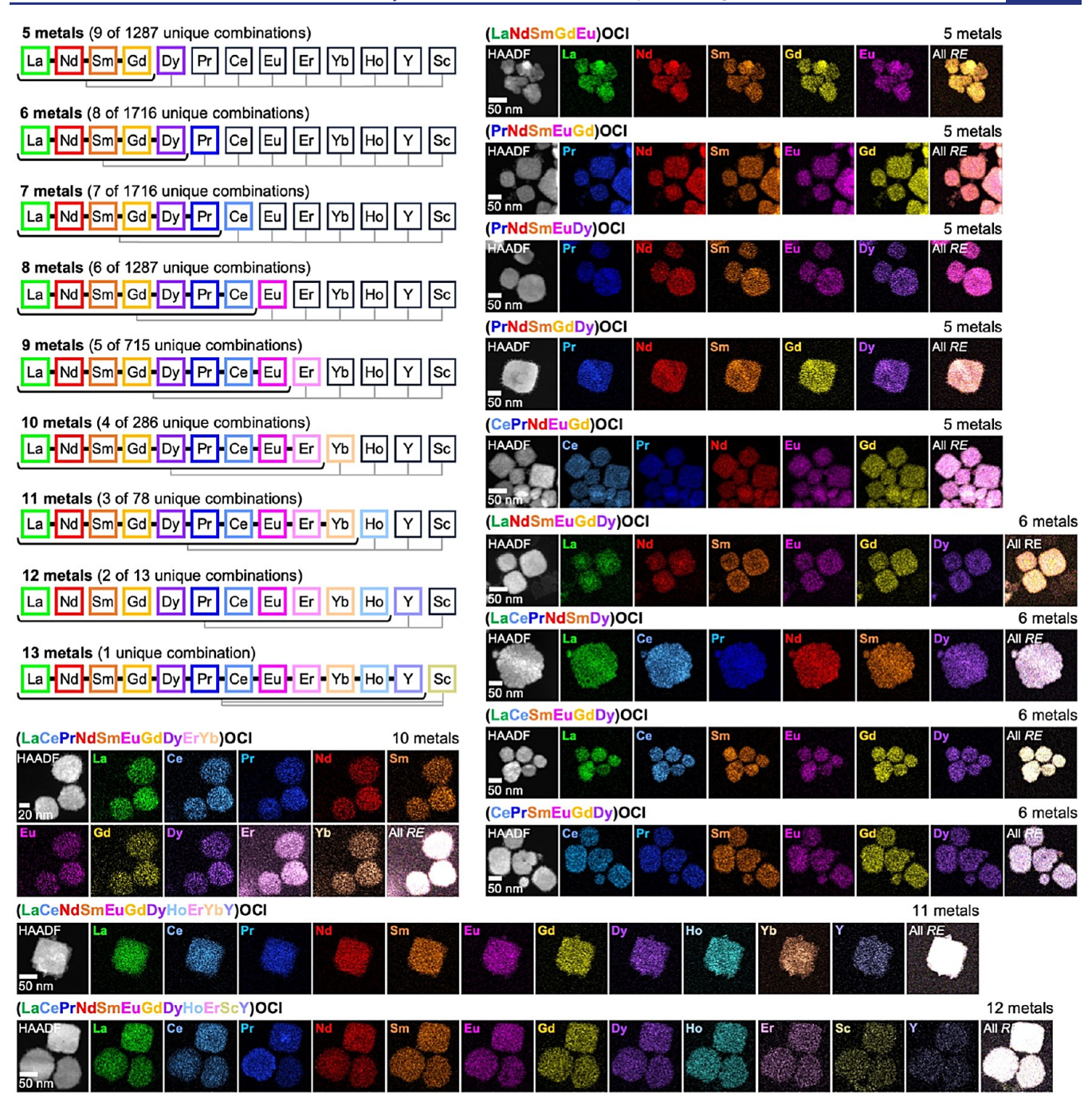


Figure 8. High-entropy *REOC*l nanoparticle library. The upper left region shows a diagram that defines the 7099-member library of high-entropy *REOC*l nanoparticles based on all possible combinations of 5 through 13 rare earth metals. The diagram demonstrates how just 45 of the 7099 possible unique combinations can be constructed; the number of other unique combinations, which can be constructed in an analogous way, is also shown. The remainder of the figures shows HAADF-STEM images and corresponding STEM-EDS element maps for several additional members of this high-entropy *REOC*l nanoparticle library beyond those shown in earlier figures; more examples are included in the Supporting Information. The samples shown here include five 5-metal compositions, four 6-metal compositions, and one each having 10, 11, and 12 metals.

next shell contains predominantly (Sm,Dy)OCl; for SmOCl and DyOCl, the $\Delta H_{\rm f}^{\,\circ}$ values are -237.1 and -235.9 kcal/mol, respectively. The outer shell contains the highest proportion of GdOCl, for which $\Delta H_{\rm f}^{\,\circ}$ is -234.0 kcal/mol. S8-61 Therefore, the progression from the center to the outer edge of the core@ shell@shell intermediate follows the trend of increasing formation enthalpies, suggesting that the most exothermic compound (LaOCl) forms in the core, and then the others grow, roughly in order of increasing formation enthalpy, outward from the core. Once the core@shell@shell inter-

mediate is formed, continued heating facilitates interdiffusion (perhaps driven by a high entropy of mixing) that ultimately produces the homogeneously mixed high-entropy *REOCl* phase.

Synthetic Roadmap to a 7099-Member REOCI Nanoparticle Library. Now that we understand how the REOCI nanoparticles form and demonstrated the successful synthesis of various REOCI phases, we turn to the challenge of generalizability and scope. Given that up to 13 rare earth elements can be incorporated into the REOCI nanoparticles,

we can define the potential scope by considering how many distinct high-entropy REOCl nanoparticles would be possible to synthesize. If we consider a high-entropy REOCl phase to contain five or more rare earth metals in equimolar ratios, we can propose a 7099-member library of all possible REOCl nanoparticles containing 5, 6, 7, 8, 9, 10, 11, 12, and 13 rare earth metals and for which synthetically feasible pathways exist based on the knowledge and capabilities defined in the preceding sections. (Additional compositions are also possible by shifting away from equimolar ratios, but for simplicity, these possibilities are not considered here.) Figure 8 shows part of this high-entropy REOCl nanoparticle library; details of the complete library are included in the Supporting Information. If we consider all equimolar 5-metal combinations that can be constructed from the 13 available metals, without repeating any and not taking stoichiometry variations into account, we get 1287 possible REOCl compositions. Figure 8 shows 9 of these possibilities. Keeping the first four elements constant (La, Nd, Sm, and Gd) from among the 13 possible rare earth metals, we can add one more from the remaining 9 to form 9 five-membered REOCl phases. The first, (LaNdSmGdDy)OCl, is the one we already made and is discussed in Figures 5 and 6, and the other eight are (LaNdSmGdPr)OCl, (LaNdSm-GdCe)OCl, (LaNdSmGdEu)OCl, (LaNdSmGdEr)OCl, (LaNdSmGdYb)OCl, (LaNdSmGdHo)OCl, (LaNdSmGdY)-OCl, and (LaNdSmGdSc)OCl that we synthesized and are characterized in Figure 8 and Figure S8. The remaining members of the 5-metal high-entropy REOCl nanoparticle library, beyond these nine, include all other unique 5-metal combinations from among the 13 available rare earth elements. In addition to (LaNdSmGdDy)OCl from Figures 5 and 6, we synthesized and characterized 11 additional 5-metal REOCl nanoparticles: (PrNdSmEuGd)OCl, (PrNdSmEuDy)OCl, (PrNdSmGdDy)OCl, (PrSmEuGdDy)OCl, (PrNdSmEuHo)-OCl, (PrNdSmDyHo)OCl, (CePrNdSmGd)OCl, (CePrNd-SmDy)OCl, (CePrNdEuGd)OCl, (CePrNdEuGd)OCl, and (LaCePrSmY)OCl. Data for each of these are included in Figure 8 and Figure S9.

Similarly, 1716 unique equimolar 6-metal combinations of the 13 rare earth elements are possible. Building on the 5-metal (LaNdSmGdDy)OCl, the inclusion of one additional metal leads to eight 6-metal derivatives: (LaNdSmGdDyPr)OCl, (LaNdSmGdDyCe)OCl, (LaNdSmGdDyEu)OCl, (LaNdSm-GdDyEr)OCl, (LaNdSmGdDyYb)OCl, (LaNdSmGdDyHo)-OCl, (LaNdSmGdDyY)OCl, and (LaNdSmGdDySc)OCl. The remaining equimolar 6-metal combinations, of which there are 1708, comprise all additional unique 6-metal combinations from among the 13 available rare earth elements. Figure 8 and Figure S10 include experimental data for seven additional 6-metal high-entropy REOCl nanoparticles, in addition to (LaCeNdSmGdDy)OCl, which is included in Figure 6. Similar rationale can be applied to mapping out all unique equimolar combinations containing 7, 8, 9, 10, 11, 12, and 13 rare earth metals, as shown in Figure 8. (LaNd-SmGdDyPrCeEuErYbHoYSc)OCl, shown in Figure 1, is the only member that contains all 13 of our constituent rare earth metals. Added together, there are 7099 unique equimolar combinations that contain between 5 and 13 rare earth metals in the REOCl nanoparticles based on projected synthetic feasibility. Altogether, in Figure 8 and Figure S11, as well as in earlier figures, we have synthesized and characterized 40 members of the 7099-member high-entropy REOCl nanoparticle library to help validate the potential scope and feasibility.

Exploration of Band Gap Energies. The availability of synthetically feasible pathways to 7099 distinct high-entropy *REOCI* nanoparticles opens the door to exploring properties across a broad scope of related materials. Comprehensive screening and in-depth investigations, given the compositional complexity of these materials, are beyond the scope of this study. However, as a first step, here, we explore the band gap energies of a subset of high-entropy *REOCI* nanoparticles and compare them to their synthetically accessible single-metal end members.

Figure 9 shows UV-visible absorption spectra, along with the corresponding Tauc plots, for the single-metal nanoparticle

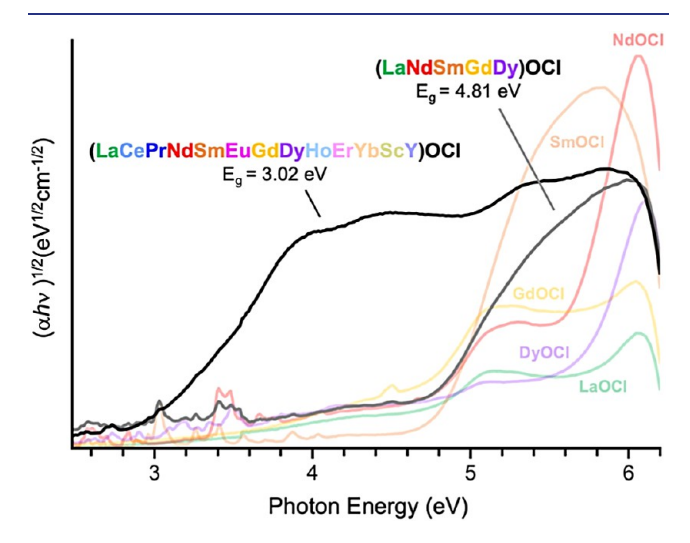


Figure 9. Optical band gap characterization for selected *REOCl* nanoparticles. A Tauc plot (based on an indirect band gap) is shown for powder samples of LaOCl, NdOCl, SmOCl, GdOCl, DyOCl, (LaNdSmGdDy)OCl, and (LaCePrNdSmEuGdDyHoErYbScY)OCl nanoparticles. The extrapolated band gaps for the high-entropy *REOCl* samples are also shown.

samples LaOCl, NdOCl, SmOCl, GdOCl, and DyOCl. Analysis of the Tauc plots for these ultrawide indirect band gap semiconductors, achieved by extrapolating the linear regions of the steep lowest-energy transition to the extrapolated baselines, 62 indicates that the band gap energies range from 4.79 eV for LaOCl to 4.85 eV for DyOCl (Figure S12). Figure 9 also shows data for the 5-metal (LaNd-SmGdDy)OCl nanoparticle sample and the 13-metal (LaCePr-NdSmEuGdDyHoErYbScY)OCl nanoparticle sample. For (LaNdSmGdDy)OCl, the band gap energy is 4.82 eV, which matches well with the weighted average of the five REOCl end members. From this analysis, there does not appear to be any significant shift in the band gap due to the mixing of five rare earth cations in the high-entropy oxychloride. However, for (LaCePrNdSmEuGdDyHoErYbScY)OCl, the band gap energy is 3.01 eV, which is much lower than the band gap of (LaNdSmGdDy)OCl, as well as the band gaps of the synthetically accessible single-metal REOCl compounds; see the Supporting Information for more details. Therefore, for the 13-metal high-entropy oxychloride, the cation mixing does appear to significantly shift the band gap to lower energies, far below the weighted average of the end members and also falling outside the range of end member band gap energies. These observations hint at the complex correlation between

composition and band gap that may exist for high-entropy materials having unusually large numbers of cations randomized within the structure, especially for combined multication/multianion compounds. ^{23,29}

CONCLUSIONS

In conclusion, we established a synthetic roadmap to a 7099member library of high-entropy REOCl nanoparticles, along with an oxybromide analogue. The ability to synthesize 40 members of this REOCl nanoparticle library-including 5metal (LaNdSmGdDy)OCl, 13-metal (LaCePrNdSm-EuGdDyHoErYbScY)OCl, and other 5-, 6-, 7-. 8-, 9-, 10-, 11-, and 12-metal combinations—experimentally demonstrates and validates the mix-and-match compositional tunability that can be achieved. Time point studies revealed the unexpected finding that core@shell@shell intermediates form in situ, en route to the final high-entropy nanoparticles. These insights into the formation pathway help to inform how targeted highentropy compositions may be accessed and tuned in this and related systems. As an important complement to synthesis, the compositional scope of the library allowed us to address characterization challenges involving the deconvolution of a large number of closely spaced and overlapping X-ray energy lines during EDS analysis, which is foundational for analyzing samples of high-entropy nanoparticles. To do so, we used the capabilities of the REOCl nanoparticle library to design and synthesize several sets of control samples to evaluate the reliability of mainstream compositional analysis strategies. Upon systematic removal of individual elements from an EDS model, we observed changes in the simulated spectrum that differed from the experimental spectrum, indicating that EDS spectra for each high-entropy composition serve as a fingerprint that can uniquely identify it. By comparing physical mixtures of individual REOCl nanoparticles with high-entropy REOCl nanoparticles having the same constituent elements, we validated that the elements were homogeneously mixed. By synthesizing REOCl samples having strategic compositions that systematically progressed from 13 rare earth elements to only one, we were able to validate both compositional tunability and reliable analysis due to good agreement between simulated and experimental EDS spectra.

Given the broad range of compositions that can be accessed in this large library of high-entropy REOCl nanoparticles, we also carried out preliminary evaluation of the band gap energies for the 5-metal (LaNdSmGdDy)OCl and 13-metal (LaCePrNdSmEuGdDyHoErYbScY)OCl samples. (LaNd-SmGdDy)OCl had a band gap energy that corresponded well with the weighted average of the end members, but the band gap for (LaCePrNdSmEuGdDyHoErYbScY)OCl was significantly narrower than those of the synthetically accessible end members. This initial screening motivates further in-depth analysis of how composition, along with the number of elements in a high-entropy compound, influences band gap energies. Such efforts are especially interesting for multication/ multianion systems like REOCl, where potentially competing and contradictory effects can influence properties in unknown and unexpected ways. 23,29 More broadly, the compositional tunability inherent in this system, coupled with the broad scope of synthetically accessible products, aligns well with the growing need for library-level synthetic platforms. 63-70 Integration with automated platforms driven by artificial intelligence (AI) and robotics, which are anticipated to expand

capabilities in materials screening and discovery, could further expand the applicability of library-level synthesis.^{71–75}

■ EXPERIMENTAL SECTION

Chemicals. The following chemicals were obtained from Sigma-Aldrich: cerium chloride heptahydrate (CeCl₃·7H₂O, 99.99%), neodymium chloride hexahydrate (NdCl₃·6H₂O, 99.9%), gadolinium chloride hexahydrate (GdCl₃·6H₂O, 99%), erbium chloride hexahydrate (ErCl₃·6H₂O, 99.9%), ytterbium chloride hexahydrate (YbCl₃· 7H₂O, 99.998%), scandium chloride hexahydrate (ScCl₃·6H₂O, 99.9%), dysprosium bromide hydrate (DyBr₃·H₂O, 99.9%), and oleylamine (t-OLAM, 70%, technical grade). The following chemicals were obtained from Alfa Aesar: yttrium chloride hydrate (YCl₃·H₂O, 99.9%) and gadolinium bromide hydrate (GdBr₃·H₂O, 99.99%). The following chemicals were obtained from Thermo Scientific: lanthanum chloride heptahydrate (LaCl₃·7H₂O, 99.99%), samarium chloride hydrate (SmCl₃·H₂O, 99.9%), europium chloride hexahydrate (EuCl₃·6H₂O, 99.9%), dysprosium chloride hydrate (DyCl₃· H₂O, 99.9%), holmium chloride hexahydrate (HoCl₃·6H₂O, 99.9%), neodymium bromide hydrate (NdBr₃·H₂O, 99.9%), and samarium bromide hexahydrate (SmBr $_3$ ·6H $_2$ O, 99.9 $\stackrel{-}{9}$). The following chemicals were obtained from STREM Chemicals: praseodymium chloride heptahydrate (PrCl₃·7H₂O, 99.9%) and lanthanum bromide heptahydrate (LaBr₃·7H₂O, 99.9%). All solvents (hexanes, toluene, methanol, and ethanol) were of analytical grade. All of the above chemicals were used as received without further purification.

Synthesis of REOX Nanoparticles. To target near-equimolar REOX compositions, appropriate molar ratios (Table S1 and S2) of each REX3 were mixed in a precursor salt solution in 10 mL of t-OLAM in a 20 mL septum capped vial to target a 0.05 M REX₃ solution; see the sample calculation in the Supporting Information. This salt solution was heated to 140 °C on a hot plate and stirred with a stir bar for 1 h. At the same time, 10 mL of t-OLAM was placed under vacuum in a 100 mL three-necked round-bottom flask and heated at 120 $^{\circ}\text{C}$ for 1 h. The flask was equipped with a thermometer, a condenser column, a magnetic stir bar, and a rubber septum. After 1 h, the salt solution and round-bottom flask were each cycled three times between vacuum and argon and were eventually left under a blanket of argon. The temperature of t-OLAM in the round-bottom flask was raised to 330 °C over the course of 15 min. Upon reaching 330 °C, the contents of the vial containing the salt solution in t-OLAM were swiftly injected into the round-bottom flask, and the reaction temperature dropped to 270 °C. Once the reaction flask returned to a temperature of 330 °C, the reaction was held for 1 h. The reaction mixture was cooled by removing the heating mantle, blowing air on the flask until it reached 200 °C, and then placed in a water bath until it reached room temperature. The product was precipitated by adding methanol and then centrifuging. The product was washed two times in total by being resuspended in toluene, precipitated with methanol, and then centrifuged. The product was resuspended in hexanes and transferred to a vial for storage and characterization. In the case of the time point studies, the previous procedure was used, except that the reaction temperature was adjusted to 270 °C and the reaction time was either 5, 10, or 15 min. The precursor salts used with the time point study were LaCl₃·7H₂O, NdCl₃·6H₂O, SmCl₃·H₂O, GdCl₃·6H₂O, and DyCl₃·H₂O.

Powder X-ray Diffraction. Powder X-ray diffraction (XRD) data were collected on an Empyrean X-ray diffractometer by using Cu $K\alpha$ radiation. Nanoparticle samples were deposited on a zero background Si sample holder. Crystal structures were simulated using Crystal-Maker, and reference patterns were generated using CrystalDiffract, distributed by CrystalMaker Software Ltd., Oxford, England (www.crystalmaker.com). Information about lattice parameters and crystal structure types is included in Table S3.

Scanning/Transmission Electron Microscopy. A FEI Talos F200X S/TEM operating at an accelerating voltage of 200 kV was used to collect high-resolution transmission electron microscopy (HRTEM) images, high angle annular dark field scanning transmission electron microscopy (HAADF-STEM) images, and STEM

energy dispersive X-ray spectroscopy (STEM-EDS) element maps. Each sample was suspended and sonicated in a hexanes/t-OLÂM mixture for 30 min and then drop-cast on a Au grid. Velox 3.6.0 software was used to analyze the STEM-EDS element map data. The EDS lines mapped were the L series for La, Ce, Pr, Nd, Sm, Eu, Gd, Dy, Ho, Er, and Yb and the K series for Sc, Y, and Cl. Prefiltering, postfiltering, and Brown-Powell ionization cross-sectional modeloptimized spectrum fitting were conducted on the net elemental map data. Quantification data for La, Ce, Pr, Nd, Sm, Eu, Gd, Dy, Ho, Er, Yb, Sc, Y, Cl, and Au were generated by using spectrum integration across the particle region in each map. The Au signal was included in the quantification, as otherwise, the Yb signal can be erroneously high due to its close overlap with Au; the Au signal was then subtracted out of the total to give accurate quantification of the rare earth elements. The integrated spectrum was analyzed with the inclusion of the elements La, Ce, Pr, Nd, Sm, Eu, Gd, Dy, Ho, Er, Yb, Sc, Y, Cl, Au, Al, Si, C, O, Zr, Cu, and Ni to account for any "phantom" background signals within the EDS spectra. The experimental data, the simulated spectrum generated by the software, and the EDS quantification lines that make up the reference were exported and plotted to generate the data in the figures. All stated elements were used in the analysis of all samples, unless otherwise indicated for specific experiments (i.e., exclusions of certain elements and the analysis of the sample containing a physical mixture of particles). ImageJ was used to perform particle size and lattice parameter analyses of HRTEM and STEM images.

Diffuse Reflectance Spectroscopy. Diffuse reflectance spectra were obtained on an Agilent/Cary 7000 UV—visible spectrometer equipped with a 150 mm integrating sphere in diffuse reflection mode. Spectra were collected from 200 to 500 nm, with 1 nm steps. Dried nanoparticle samples were placed in a microsample cup for measurement. The reference spectrum for total reflectance was measured against a KBr standard. Plots of the Kubelka—Munk function, raised to the power of 1/2 (direct band gap) versus energy in eV, were constructed. Band gaps were calculated by fitting the linear region at the onset of absorption and extrapolating to the *x*-intercept.

ASSOCIATED CONTENT

Supporting Information

The Supporting Information is available free of charge at https://pubs.acs.org/doi/10.1021/jacs.4c06413.

Expanded description of the high-entropy REOCl library; additional XRD, TEM, and STEM-EDS data; Tauc plot analysis; additional experimental details; additional lattice constant information (PDF)

AUTHOR INFORMATION

Corresponding Author

Raymond E. Schaak — Department of Chemistry and Materials Research Institute, The Pennsylvania State University, University Park, Pennsylvania 16802, United States; Department of Chemical Engineering, The Pennsylvania State University, University Park, Pennsylvania 16802, United States; orcid.org/0000-0002-7468-8181; Email: res20@psu.edu

Author

Charles H. Wood – Department of Chemistry, The Pennsylvania State University, University Park, Pennsylvania 16802, United States

Complete contact information is available at: https://pubs.acs.org/10.1021/jacs.4c06413

Notes

The authors declare no competing financial interest.

ACKNOWLEDGMENTS

This work was supported primarily by the Penn State Materials Research Science and Engineering Center Center for Nanoscale Science under National Science Foundation award DMR-2011839. Additional partial support (for the initial discovery of a 5-metal *REOCl*) was provided by the U.S. National Science Foundation under grant CHE-2203353. TEM, XRD, and UV—vis data were acquired at the Materials Characterization Lab of the Penn State Materials Research Institute. C.H.W. thanks Samuel Soliman for the initial suggestion to synthesize highentropy rare earth oxyhalides.

REFERENCES

- (1) Sun, Y.; Dai, S. High-Entropy Materials for Catalysis: A New Frontier. Sci. Adv. 2021, 7 (20), No. eabg1600.
- (2) Xin, Y.; Li, S.; Qian, Y.; Zhu, W.; Yuan, H.; Jiang, P.; Guo, R.; Wang, L. High-Entropy Alloys as a Platform for Catalysis: Progress, Challenges, and Opportunities. ACS Catal. 2020, 10 (19), 11280–11306.
- (3) Theibault, M. J.; McCormick, C. R.; Lang, S.; Schaak, R. E.; Abruña, H. D. High Entropy Sulfide Nanoparticles as Lithium Polysulfide Redox Catalysts. *ACS Nano* **2023**, *17* (18), 18402–18410.
- (4) Zeng, Y.; Ouyang, B.; Liu, J.; Byeon, Y. W.; Cai, Z.; Miara, L. J.; Wang, Y.; Ceder, G. High-Entropy Mechanism to Boost Ionic Conductivity. *Science* **2022**, *378* (6626), 1320–1324.
- (5) Pavithra, C. L. P.; Janardhana, R. K. S. K.; Reddy, K. M.; Murapaka, C.; Joardar, J.; Sarada, B. V.; Tamboli, R. R.; Hu, Y.; Zhang, Y.; Wang, X.; Dey, S. R. An Advancement in the Synthesis of Unique Soft Magnetic CoCuFeNiZn High Entropy Alloy Thin Films. *Sci. Rep.* **2021**, *11* (1), 1–8.
- (6) Wang, X.; Yao, H.; Zhang, Z.; Li, X.; Chen, C.; Yin, L.; Hu, K.; Yan, Y.; Li, Z.; Yu, B.; Cao, F.; Liu, X.; Lin, X.; Zhang, Q. Enhanced Thermoelectric Performance in High Entropy Alloys Sn0.25Pb0.25Mn0.25Ge0.25Te. ACS Appl. Mater. Interfaces 2021, 13 (16), 18638–18647.
- (7) Yeh, J. W.; Chen, S. K.; Lin, S. J.; Gan, J. Y.; Chin, T. S.; Shun, T. T.; Tsau, C. H.; Chang, S. Y. Nanostructured High-Entropy Alloys with Multiple Principal Elements: Novel Alloy Design Concepts and Outcomes. *Adv. Eng. Mater.* **2004**, *6* (5), 299–303.
- (8) Cantor, B.; Chang, I. T. H.; Knight, P.; Vincent, A. J. B. Microstructural Development in Equiatomic Multicomponent Alloys. *Mater. Sci. and Eng.: A* **2004**, *375*–377, 213–218.
- (9) Löffler, T.; Savan, A.; Garzón-Manjón, A.; Meischein, M.; Scheu, C.; Ludwig, A.; Schuhmann, W. Toward a Paradigm Shift in Electrocatalysis Using Complex Solid Solution Nanoparticles. *ACS Energy Lett.* **2019**, *4* (5), 1206–1214.
- (10) Ching, W. Y.; San, S.; Brechtl, J.; Sakidja, R.; Zhang, M.; Liaw, P. K. Fundamental Electronic Structure and Multiatomic Bonding in 13 Biocompatible High-Entropy Alloys. *NPJ Comp. Mater.* **2020**, 6 (1), 45.
- (11) Leong, Z.; Wróbel, J. S.; Dudarev, S. L.; Goodall, R.; Todd, I.; Nguyen-Manh, D. The Effect of Electronic Structure on the Phases Present in High Entropy Alloys. *Sci. Rep.* **2017**, *7* (1), 39803.
- (12) Schweidler, S.; Botros, M.; Strauss, F.; Wang, Q.; Ma, Y.; Velasco, L.; Cadilha Marques, G.; Sarkar, A.; Kübel, C.; Hahn, H.; Aghassi-Hagmann, J.; Brezesinski, T.; Breitung, B. High-Entropy Materials for Energy and Electronic Applications. *Nature Rev. Mater.* **2024**, *9* (4), 266–281.
- (13) Dey, G. R.; Soliman, S. S.; McCormick, C. R.; Wood, C. H.; Katzbaer, R. R.; Schaak, R. E. Colloidal Nanoparticles of High Entropy Materials: Capabilities, Challenges, and Opportunities in Synthesis and Characterization. *ACS Nanoscience Au* **2024**, *4* (1), 3–20.
- (14) Kar, N.; McCoy, M.; Wolfe, J.; Bueno, S. L. A.; Shafei, I. H.; Skrabalak, S. E. Retrosynthetic Design of Core—Shell Nanoparticles for Thermal Conversion to Monodisperse High-Entropy Alloy Nanoparticles. *Nature Synthesis* **2024**, 3 (2), 175–184.

- (15) Saldanha, P. L.; Lesnyak, V.; Manna, L. Large Scale Syntheses of Colloidal Nanomaterials. *Nano Today* **2017**, *12*, 46–63.
- (16) Zhang, R. Z.; Reece, M. J. Review of High Entropy Ceramics: Design, Synthesis, Structure and Properties. *J. Mater. Chem. A Mater.* **2019**, 7 (39), 22148–22162.
- (17) Wang, B.; Wang, C.; Yu, X.; Cao, Y.; Gao, L.; Wu, C.; Yao, Y.; Lin, Z.; Zou, Z. General Synthesis of High-Entropy Alloy and Ceramic Nanoparticles in Nanoseconds. *Nature Synthesis* **2022**, *1* (2), 138–146.
- (18) Yao, Y.; Huang, Z.; Xie, P.; Lacey, S. D.; Jacob, R. J.; Xie, H.; Chen, F.; Nie, A.; Pu, T.; Rehwoldt, M.; Yu, D.; Zachariah, M. R.; Wang, C.; Shahbazian-Yassar, R.; Li, J.; Hu, L. Carbothermal Shock Synthesis of High-Entropy-Alloy Nanoparticles. *Science* **2018**, 359 (6383), 1489–1494.
- (19) Dey, G. R.; McCormick, C. R.; Soliman, S. S.; Darling, A. J.; Schaak, R. E. Chemical Insights into the Formation of Colloidal High Entropy Alloy Nanoparticles. *ACS Nano* **2023**, *17* (6), 5943–5955.
- (20) Soliman, S. S.; Dey, G. R.; McCormick, C. R.; Schaak, R. E. Temporal Evolution of Morphology, Composition, and Structure in the Formation of Colloidal High-Entropy Intermetallic Nanoparticles. *ACS Nano* **2023**, *17* (16), 16147–16159.
- (21) McCormick, C. R.; Schaak, R. E. Simultaneous Multication Exchange Pathway to High-Entropy Metal Sulfide Nanoparticles. *J. Am. Chem. Soc.* **2021**, *143* (2), 1017–1023.
- (22) Shi, Y.; Xu, Q.; Tian, Z.; Liu, G.; Ma, C.; Zheng, W. Ionic Liquid-Hydroxide-Mediated Low-Temperature Synthesis of High-Entropy Perovskite Oxide Nanoparticles. *Nanoscale* **2022**, *14* (21), 7817–7827.
- (23) Ward-O'Brien, B.; McNaughter, P. D.; Cai, R.; Chattopadhyay, A.; Flitcroft, J. M.; Smith, C. T.; Binks, D. J.; Skelton, J. M.; Haigh, S. J.; Lewis, D. J. Quantum Confined High-Entropy Lanthanide Oxysulfide Colloidal Nanocrystals. *Nano Lett.* **2022**, 22 (20), 8045–8051.
- (24) Wu, D.; Kusada, K.; Nanba, Y.; Koyama, M.; Yamamoto, T.; Toriyama, T.; Matsumura, S.; Seo, O.; Gueye, I.; Kim, J.; Rosantha Kumara, L. S.; Sakata, O.; Kawaguchi, S.; Kubota, Y.; Kitagawa, H. Noble-Metal High-Entropy-Alloy Nanoparticles: Atomic-Level Insight into the Electronic Structure. *J. Am. Chem. Soc.* **2022**, *144* (8), 3365–3369.
- (25) Minamihara, H.; Kusada, K.; Wu, D.; Yamamoto, T.; Toriyama, T.; Matsumura, S.; Kumara, L. S. R.; Ohara, K.; Sakata, O.; Kawaguchi, S.; Kubota, Y.; Kitagawa, H. Continuous-Flow Reactor Synthesis for Homogeneous 1 Nm-Sized Extremely Small High-Entropy Alloy Nanoparticles. *J. Am. Chem. Soc.* **2022**, *144* (26), 11525–11529.
- (26) Hanabata, S.; Kusada, K.; Yamamoto, T.; Toriyama, T.; Matsumura, S.; Kawaguchi, S.; Kubota, Y.; Nishida, Y.; Haneda, M.; Kitagawa, H. Denary High-Entropy Oxide Nanoparticles Synthesized by a Continuous Supercritical Hydrothermal Flow Process. *J. Am. Chem. Soc.* **2024**, *146* (1), 181–186.
- (27) Broge, N. L. N.; Bondesgaard, M.; Søndergaard-Pedersen, F.; Roelsgaard, M.; Iversen, B. B. Autocatalytic Formation of High-Entropy Alloy Nanoparticles. *Angew. Chem., Int. Ed.* **2020**, *59* (49), 21920–21924.
- (28) Bueno, S. L. A.; Leonardi, A.; Kar, N.; Chatterjee, K.; Zhan, X.; Chen, C.; Wang, Z.; Engel, M.; Fung, V.; Skrabalak, S. E. Quinary, Senary, and Septenary High Entropy Alloy Nanoparticle Catalysts from Core@Shell Nanoparticles and the Significance of Intraparticle Heterogeneity. *ACS Nano* **2022**, *16* (11), 18873–18885.
- (29) Ward-O'brien, B.; Pickering, E. J.; Ahumada-Lazo, R.; Smith, C.; Zhong, X. L.; Aboura, Y.; Alam, F.; Binks, D. J.; Burnett, T. L.; Lewis, D. J. Synthesis of High Entropy Lanthanide Oxysulfides via the Thermolysis of a Molecular Precursor Cocktail. *J. Am. Chem. Soc.* **2021**, *143* (51), 21560–21566.
- (30) Zulkiflee, A.; Khan, M. M.; Harunsani, M. H. Bismuth Oxyhalides: Recent Progress and Its Applications in Photocatalysis, Hydrogen Production, Antibacterial Studies, and Sensors. *Mater. Sci. Semiconductor Process* **2023**, *163*, No. 107547.

- (31) Long, J. P.; Wan, Z.; Yan, X. G.; Huang, W. Q.; Huang, G. F.; Peng, P. Band Gap Engineering by Lanthanide Doping in the Photocatalyst LaOF: First-Principles Study. *Int. J. of Mod. Phys. B* **2014**, 28 (11), 1450069.
- (32) Waetzig, G. R.; Horrocks, G. A.; Davidson, R. D.; Jude, J. W.; Villalpando, G. V.; Zuin, L.; Banerjee, S. In a Different Light: Deciphering Optical and X-Ray Sensitization Mechanisms in an Expanded Palette of LaOCl Phosphors. *J. Phys. Chem. C* **2018**, *122* (28), 16412–16423.
- (33) Du, Y. P.; Zhang, Y. W.; Sun, L. D.; Yan, C. H. Luminescent Monodisperse Nanocrystals of Lanthanide Oxyfluorides Synthesized from Trifluoroacetate Precursors in High-Boiling Solvents. *J. Phys. Chem. C* 2008, *112* (2), 405–415.
- (34) Rambabu, U.; Mathur, A.; Buddhudu, S. Fluorescence Spectra of Eu³⁺ and Tb³⁺-Doped Lanthanide Oxychloride Powder Phosphors. *Mater. Chem. Phys.* **1999**, *61* (2), 156–162.
- (35) Udayakantha, M.; Handy, J. V.; Davidson, R. D.; Kaur, J.; Villalpando, G.; Zuin, L.; Chakraborty, S.; Banerjee, S. Halide Replacement with Complete Preservation of Crystal Lattice in Mixed-Anion Lanthanide Oxyhalides. *Angew. Chem., Int. Ed.* **2021**, *60* (28), 15582–15589.
- (36) Udayakantha, M.; Schofield, P.; Waetzig, G. R.; Banerjee, S. A Full Palette: Crystal Chemistry, Polymorphism, Synthetic Strategies, and Functional Applications of Lanthanide Oxyhalides. *J. Solid State Chem.* **2019**, 270, 569–592.
- (37) Templeton, D. H.; Dauben, C. H. Crystal Structures of Rare Earth Oxychlorides. J. Am. Chem. Soc. 1953, 75 (23), 6069–6070.
- (38) Zachariasen, W. H. IUCr. Crystal Chemical Studies of the Sf-Series of Elements. XII. New Compounds Representing Known Structure Types. *Acta Crystallogr.* **1949**, 2 (6), 388–390.
- (39) Gouget, G.; Pellerin, M.; Pautrot-D'Alençon, L.; Le Mercier, T.; Murray, C. B. Efficient Photoluminescence of Isotropic Rare-Earth Oxychloride Nanocrystals from a Solvothermal Route. *Chem. Commun.* **2020**, *56* (23), 3429–3432.
- (40) Renero-Lecuna, C.; Herrero, A.; Jimenez de Aberasturi, D.; Martínez-Flórez, M.; Valiente, R.; Mychinko, M.; Bals, S.; Liz-Marzán, L. M. Nd³⁺-Doped Lanthanum Oxychloride Nanocrystals as Nanothermometers. *J. Phys. Chem. C* **2021**, *125* (36), 19887–19896.
- (41) Tamura, S.; Kato, Y.; Imanaka, N. Ionic Conducting Properties in LaOCl–LaOBr Solid Solutions. *J. Alloys Compd.* **2006**, 408–412, 653–656.
- (42) Imanaka, N.; Okamoto, K.; Adachi, G. Y. Water-Insoluble Lanthanum Oxychloride-Based Solid Electrolytes with Ultra-High Chloride Ion Conductivity. *Anewg. Chem., Int. Ed.* **2002**, *41* (20), 3890–3892.
- (43) Au, C. T.; He, H.; Lai, S. Y.; Ng, C. F. The Oxidative Coupling of Methane over BaCO₃/LaOBr—Catalysts of High Ethylene Yield. *J. Catal.* **1996**, *16*3 (2), 399–408.
- (44) Wei, Z. X.; Wang, Y.; Zhang, X. J.; Hu, C. W. Combustion Synthesis and Effect of LaMnO₃ and LaOCl Powder Mixture on HMX Thermal Decomposition. *Thermochim. Acta* **2010**, 499 (1–2), 111–116.
- (45) Podkolzin, S. G.; Stangland, E. E.; Jones, M. E.; Peringer, E.; Lercher, J. A. Methyl Chloride Production from Methane over Lanthanum-Based Catalysts. *J. Am. Chem. Soc.* **2007**, *129* (9), 2569–2576.
- (46) Kim, D.; Park, S.; Kim, S.; Kang, S. G.; Park, J. C. Blue-Emitting Eu²⁺-Activated LaOX (X = Cl, Br, and I) Materials: Crystal Field Effect. *Inorg. Chem.* **2014**, 53 (22), 11966–11973.
- (47) Osanloo, M. R.; Van de Put, M. L.; Saadat, A.; Vandenberghe, W. G. Identification of Two-Dimensional Layered Dielectrics from First Principles. *Nat. Commun.* **2021**, *12* (1), 5051.
- (48) Katzbaer, R. R.; dos Santos Vieira, F. M.; Dabo, I.; Mao, Z.; Schaak, R. E. Band Gap Narrowing in a High-Entropy Spinel Oxide Semiconductor for Enhanced Oxygen Evolution Catalysis. *J. Am. Chem. Soc.* **2023**, *145* (12), 6753–6761.
- (49) Sarkar, A.; Loho, C.; Velasco, L.; Thomas, T.; Bhattacharya, S. S.; Hahn, H.; Djenadic, R. Multicomponent Equiatomic Rare Earth

- Oxides with a Narrow Band Gap and Associated Praseodymium Multivalency. Dalt. Trans. 2017, 46 (36), 12167–12176.
- (50) Sarkar, A.; Eggert, B.; Velasco, L.; Mu, X.; Lill, J.; Ollefs, K.; Bhattacharya, S. S.; Wende, H.; Kruk, R.; Brand, R. A.; Hahn, H. Role of Intermediate 4f States in Tuning the Band Structure of High Entropy Oxides. *APL Mater.* **2020**, *8* (5), No. 051111.
- (51) Yao, Y.; Dong, Q.; Brozena, A.; Luo, J.; Miao, J.; Chi, M.; Wang, C.; Kevrekidis, I. G.; Ren, Z. J.; Greeley, J.; Wang, G.; Anapolsky, A.; Hu, L. High-Entropy Nanoparticles: Synthesis-Structureproperty Relationships and Data-Driven Discovery. *Science* 2022, 376 (6589), No. eabn3103.
- (52) Sun, Y.; Zhang, W.; Zhang, Q.; Li, Y.; Gu, L.; Guo, S. A General Approach to High-Entropy Metallic Nanowire Electrocatalysts. *Matter* **2023**, *6* (1), 193–205.
- (53) Al Zoubi, W.; Putri, R. A. K.; Abukhadra, M. R.; Ko, Y. G. Recent Experimental and Theoretical Advances in the Design and Science of High-Entropy Alloy Nanoparticles. *Nano Energy* **2023**, *110*, No. 108362.
- (54) Wood, C. H.; Schaak, R. E. Topochemical Anionic Subunit Insertion Reaction for Constructing Nanoparticles of Layered Oxychalcogenide Intergrowth Structures. *J. Am. Chem. Soc.* **2023**, 145 (34), 18711–18715.
- (55) Hölsä, J.; Lastusaari, M.; Valkonen, J. X-Ray Powder Diffraction Study of the Stability of Solid Solutions in LaO($Cl_{1-x}Br_x$). *J. Alloys Compd.* **1997**, 262–263, 299–304.
- (56) Holder, C. F.; Schaak, R. E. Tutorial on Powder X-Ray Diffraction for Characterizing Nanoscale Materials. *ACS Nano* **2019**, 13 (7), 7359–7365.
- (57) Gao, S.; Hao, S.; Huang, Z.; Yuan, Y.; Han, S.; Lei, L.; Zhang, X.; Shahbazian-Yassar, R.; Lu, J. Synthesis of High-Entropy Alloy Nanoparticles on Supports by the Fast Moving Bed Pyrolysis. *Nat. Commun.* **2020**, *11* (1), 2016.
- (58) Hisham, M. W. M.; Benson, S. W. Thermochemistry of Inorganic Solids. 3. Enthalpies of Formation of Solid Metal Oxyhalide Compounds. *J. Phys. Chem.* **1986**, *90* (5), 885–888.
- (59) Jacob, K. T.; Dixit, A.; Rajput, A. Stability Field Diagrams for Ln-O-Cl Systems. *Bull. of Mater. Sci.* **2016**, *39* (3), 603–611.
- (60) Struck, C. W.; Baglio, J. A. Estimates for the Enthalpy of Formation of Rare-Earth Oxyhalides with the P4/nmm Structure. *Thermochim. Acta* **1993**, 216 (C), 45–79.
- (61) Navrotsky, A.; Yang, S.; Anderko, A.; Riman, R. E. Thermochemistry of 3D and 2D Rare Earth Oxychlorides (REOCls). *Inorg. Chem.* **2022**, *61* (19), 7590–7596.
- (62) Makuła, P.; Pacia, M.; Macyk, W. How To Correctly Determine the Band Gap Energy of Modified Semiconductor Photocatalysts Based on UV-Vis Spectra. *J. Phys. Chem. Letters* **2018**, 9 (23), 6814–6817
- (63) Fenton, J. L.; Steimle, B. C.; Schaak, R. E. Tunable Intraparticle Frameworks for Creating Complex Heterostructured Nanoparticle Libraries. *Science* **2018**, *360* (6388), 513–517.
- (64) Steimle, B. C.; Fenton, J. L.; Schaak, R. E. Rational Construction of a Scalable Heterostructured Nanorod Megalibrary. *Science* **2020**, 367 (6476), 418–424.
- (65) Schaak, R. E.; Steimle, B. C.; Fenton, J. L. Made-to-Order Heterostructured Nanoparticle Libraries. *Acc. Chem. Res.* **2020**, *53* (11), 2558–2568.
- (66) Choi, J. H.; Wang, H.; Oh, S. J.; Paik, T.; Sung, P.; Sung, J.; Ye, X.; Zhao, T.; Diroll, B. T.; Murray, C. B.; Kagan, C. R. Exploiting the Colloidal Nanocrystal Library to Construct Electronic Devices. *Science* **2016**, 352 (6282), 205–208.
- (67) McCormick, C. R.; Katzbaer, R. R.; Steimle, B. C.; Schaak, R. E. Combinatorial Cation Exchange for the Discovery and Rational Synthesis of Heterostructured Nanorods. *Nat. Synth.* **2023**, 2 (2), 152–161.
- (68) Smith, P. T.; Ye, Z.; Pietryga, J.; Huang, J.; Wahl, C. B.; Hedlund Orbeck, J. K.; Mirkin, C. A. Molecular Thin Films Enable the Synthesis and Screening of Nanoparticle Megalibraries Containing Millions of Catalysts. *J. Am. Chem. Soc.* **2023**, *145* (25), 14031–14043.

- (69) Lai, M.; Shin, D.; Jibril, L.; Mirkin, C. A. Combinatorial Synthesis and Screening of Mixed Halide Perovskite Megalibraries. *J. Am. Chem. Soc.* **2022**, *144* (30), 13823–13830.
- (70) Chen, P.-C.; Liu, X.; Hedrick, J. L.; Xie, Z.; Wang, S.; Lin, Q.-Y.; Hersam, M. C.; Dravid, V. P.; Mirkin, C. A. Polyelemental nanoparticles libraries. *Science* **2016**, 352, 1565–1569.
- (71) Pyzer-Knapp, E. O.; Pitera, J. W.; Staar, P. W. J.; Takeda, S.; Laino, T.; Sanders, D. P.; Sexton, J.; Smith, J. R.; Curioni, A. Accelerating Materials Discovery Using Artificial Intelligence, High Performance Computing and Robotics. *NPJ Comp. Mater.* **2022**, 8 (1), 84.
- (72) Merchant, A.; Batzner, S.; Schoenholz, S. S.; Aykol, M.; Cheon, G.; Cubuk, E. D. Scaling Deep Learning for Materials Discovery. *Nature* **2023**, *624* (7990), 80–85.
- (73) Salley, D.; Manzano, J. S.; Kitson, P. J.; Cronin, L. Robotic Modules for the Programmable Chemputation of Molecules and Materials. ACS Cent. Sci. 2023, 9 (8), 1525–1537.
- (74) Burger, B.; Maffettone, P. M.; Gusev, V. V.; Aitchison, C. M.; Bai, Y.; Wang, X.; Li, X.; Alston, B. M.; Li, B.; Clowes, R.; Rankin, N.; Harris, B.; Sprick, R. S.; Cooper, A. I. A Mobile Robotic Chemist. *Nature* **2020**, *583* (7815), 237–241.
- (75) Jiang, Y.; Salley, D.; Sharma, A.; Keenan, G.; Mullin, M.; Cronin, L. An Artificial Intelligence Enabled Chemical Synthesis Robot for Exploration and Optimization of Nanomaterials. *Sci. Adv.* **2022**, *8* (40), No. eabo2626.